Hindawi
International Journal of Energy Research
Volume 2023, Article ID 3754111, 14 pages
https://doi.org/10.1155/2023/3754111

Research Article

In Situ Synthesis of ZIF-67 Thin Films Using Low Temperature Chemical Vapor Deposition to Fabricate All-Solid-State Flexible Interdigital in-Planar Microsupercapacitors

Kai-Hsiang Lo,[1] Krishnan Shanmugam Anuratha,[2] Chia-Chin Cheng,[3] Shao-Jung Wu,[4] Horng-Yi Juan,[4] Chia-Hung Su,[4] Jeng-Yu Lin ,[2] and Chien-Kuo Hsieh [1]

[1]*Department of Materials Engineering, Center for Plasma and Thin Film Technologies, Ming Chi University of Technology, New Taipei City 24301, Taiwan*
[2]*Department of Chemical and Materials Engineering, Tunghai University, Taichung City 407224, Taiwan*
[3]*R&D Lab, SulfurScience Technology Co. Ltd., New Taipei City 24301, Taiwan*
[4]*Department of Chemical Engineering, Ming Chi University of Technology, New Taipei City 24301, Taiwan*

Correspondence should be addressed to Jeng-Yu Lin; jylin@thu.edu.tw and Chien-Kuo Hsieh; jack_hsieh@mail.mcut.edu.tw

Received 23 September 2022; Revised 29 October 2022; Accepted 4 November 2022; Published 9 February 2023

Academic Editor: Soumyendu Roy

This work describes the fabrication of a flexible all-solid-state interdigital in-planar microsupercapacitor (μSC) using the in situ synthesized ZIF-67 thin films as the interdigital finger-electrode materials, platinum (Pt) thin film as the interdigital finger-electrode current collector, laser print technology for the fabrication of interdigital patterns, and low-cost commercial polyethylene terephthalate (PET) sheet as the flexible substrates, assembled with the NaOH/PVA gel electrolyte. ZIF-67 thin films are in situ synthesized onto PET substrate by ultralow temperature (ULT) chemical vapor deposition (CVD) technology at a low temperature of 140°C. We herein report the ULT CVD approach for gas phase synthesizing ZIF-67 thin films, the exactly heating temperature can produce vaporized water steam, sublimated 2-methylimidazole (2-MIM) and cobalt(II) acetylacetonate ($Co(acac)_2$) vapors at the same time. The vaporized and sublimated gaseous precursors demonstrated molecular-level reactions, including the deprotonation of 2-MIM via water steam, and the following coordinated reactions with cobalt ions decomposed from $Co(acac)_2$, for the efficiently straightforward deposition to form the uniform ZIF-67 thin films onto the substrate surface. Herein, the integration of pattern printing, CVD depositing ZIF-67 thin films, and lift-off patterning processes demonstrated a comprehensive achievement and good compatibility to integrate MOFs into miniaturized energy-storage devices.

1. Introduction

Recently, the rapid advancement of various modern microelectronic devices, such as flexible micro displays and wearable sensors [1, 2], has pushed the development of energy-storage components of integrated rapid charged miniaturized power devices. Supercapacitors (SCs) can store electrical charge by rapid charge/discharge process of electrode/electrolyte interface, have received tremendous interest by scientific community, by virtue of their high-power density, long cycle life, simple design, safeness, and their large variety of applications [3, 4]. However, conventional SCs are usually bulky, heavy, and inflexible, and moreover the utilization of liquid electrolyte cause leakage issues, which damage the SCs under externally applied strains, such as stretching and bending, resulting in the deterioration of electrochemical performance. Obviously, conventional SCs could not be applicable for miniaturized electronic devices because of the aforementioned disadvantages. Therefore, the state-of-art microsupercapacitors (μSCs) have attracted considerable attention for powering microelectronic applications. On the other hand, most of the novel microelectronic devices are practically flexible, wearable, and directly sticking to human skin. Consequently, the development of μSCs toward

lightweight, solid-state, planar, and flexible design is essential for the prospective of microelectronic applications.

Generally, the configuration of planar μSCs can be classified into two categories [5]. The first category relates to a sandwich-type μSCs with two thin-film electrodes and a gel electrolyte stacked between the negative and positive electrodes [6–8], and the second category is the design with two interdigital electrodes and a gel electrolyte configured on the same planar platform [9–11]. Among the two types of planar μSCs configurations, interdigital configuration has better compatibility and performance than sandwiched thin-film devices due to the facile fabrication of integrating microelectronic devices and the short ion transport distance between interdigital electrodes, which promotes the charge/discharge efficiency. Nevertheless, the patterning technology of in-plane interdigital μSCs still remains the challenging, which limits their practical applications. Currently, various complex technologies are widely used for patterning the interdigital electrodes, such as photolithography technology [12, 13], ink-jet, and screen printing technologies [14, 15]. Photolithography technology delivers the perfectly patterned electrodes of excellent quality with high-production cost, complicated production process, and toxic chemical treatments and hard fabrication conditions. Even though, ink-jet and screen-printing technologies are simple and low-cost, which also having the disadvantages of slow throughput and handful fabrication issues. Thereby, the aforementioned patterned techniques of in-plane interdigital μSCs fabrication are detrimental for mass production, and therefore hinder the commercial applications of interdigital μSCs. Consequently, developing a simple, cost-effective, and well-defined patterning technology is critical for the future practices of interdigital μSCs applications. Laser-based technologies are the most common patterning methods for interdigital μSCs, including laser writing [10, 16], laser scribing and laser printing technologies [11, 17–19], and so on [20]. Among them, laser printer is widely used one, employed to print documents with a resolution of several hundreds of micrometers, which is particularly satisfied with current requirements of microdevices. For instance, Hu et al. firstly utilized commercial office laser printer for printing the sacrificed patterns of Au interdigital patterns for fabricating polyaniline-based flexible interdigital in-planar μSCs [18]. Our group also applied the commercial laser printer technique to fabricate Pt interdigital patterns and employed wet chemical approach for making hydrous ruthenium oxide-based flexible interdigital in-planar μSCs [19]. In addition, the interdigital patterns were optimized for boosting the electrochemical performance of in-planar interdigital μSCs [21]. Accordingly, laser printer technique has shown the outstanding superiorities over other technologies including low-cost, arbitrary design, and scalable production.

Metal organic frameworks (MOFs) are a class of crystalline porous materials consisting of metal ions coordinated to multitopic organic ligands [22]. MOFs are emerging materials with a wide range of applications such as energy storage, catalytic activities, and electrochemistry applications [23–27]. Recently, researchers have sought MOFs in supercapacitor energy storage devices due to their large pore volumes, high-specific surface area, and chemical turnabilities [25]. Zeolitic imidazole frameworks (ZIFs) are a famous subclass of MOFs that are easy to fabricate with owning excellent chemical and thermal properties, the architecture of ZIFs contains divalent metal cations (for example, Zn^{2+}, Co^{2+}, Fe^{2+}, or Cu^{2+}), which is tetrahedrally coordinated by imidazolate-type linkers [28]. ZIF-67 (cobalt-based ZIF), is a classic type of ZIFs that can be synthesized spontaneously at room temperature upon mixing cobalt ion precursors with methyl imidazolate ligands, ZIF-67 is employed in the various applications such as chemical separation, chemical sensing, catalysis, and energy storage [29–32]. Generally, MOF-based materials are produced as bulk powders using solvent process method, which includes more steps and binding agents, were used for coating the active materials on electrode surface. Besides, solvent process method is noneco-friendly, and thereby some researchers have utilized water steam for the fabrication of MOFs. For instance, Shi et al. employed water steam assisted conversion method for the synthesis of ZIF-8 and ZIF-67 [33]. The alternative method of solvent-free chemical vapor deposition (CVD) was reported, where the preparatory deposited oxides were exposed at the 2-methylimidazole (2-MIM) vapor in order to transform the oxide into a ZIF. Recently, Stassen et al. reported a process named "MOF-CVD" in that, they deposited ZnO films via sputtering technology or atomic-layer deposition (ALD) and ZnO was transformed to ZIF-8 by exposing ZnO in 2-MIM vapor, based on the following neutralization reaction: ZnO+2-MIM $\rightarrow$ ZIF-8 + H_2O [34]. Li et al. used electrochemical deposition method to prepare ZnO films, and then employed MOF-CVD method for the transformation of ZnO into ZIF-8 [35]. Although MOF-CVD opened the solvent-free way to fabricate ZIF thin films, it involves two-steps synthesized processes with the preparatory deposition of ZnO thin film as the template to transform into ZIFs. Thus, very few pioneers have developed template-free CVD for the in situ deposition of MOF-based thin films. For instance, Huang et al. were the first and successfully demonstrated the one-step steam-assisted CVD for in situ growing of ZIF-67 thin films onto the sapphire substrate [36].

Herein, we report the comprehensive method for the fabrication of flexible all-solid-state in-planar ZIF-67-based μSCs. In this study, we used annealed process to obtain the recrystallized polyethylene terephthalate (C-PET) sheets as the flexible substrates, fabricated the interdigital patterns by laser printer patterning process, and in situ synthesized ZIF-67 thin films via ultralow temperature (ULT) CVD technology. To the best of our knowledge, we are the first to report the in situ deposition of ZIF-67 thin films for the interdigital in-planar microsupercapacitor application. Our report shows the great potential features for fabricating MOFs thin films-based μSCs and related microfabrication applications.

2. Experimental Methods

2.1. Materials. We have used PET sheet as the substrate for the fabrication of μSCs, since it is well-known and widely used, acquired many advantages, including flexibility, strength, readily available, low-cost, and favorable for mass production. Commercial PET sheets (A4 size, 297 mm × 210 mm, DCAP4O-A900915SH, PChome Online Inc., Taiwan) were

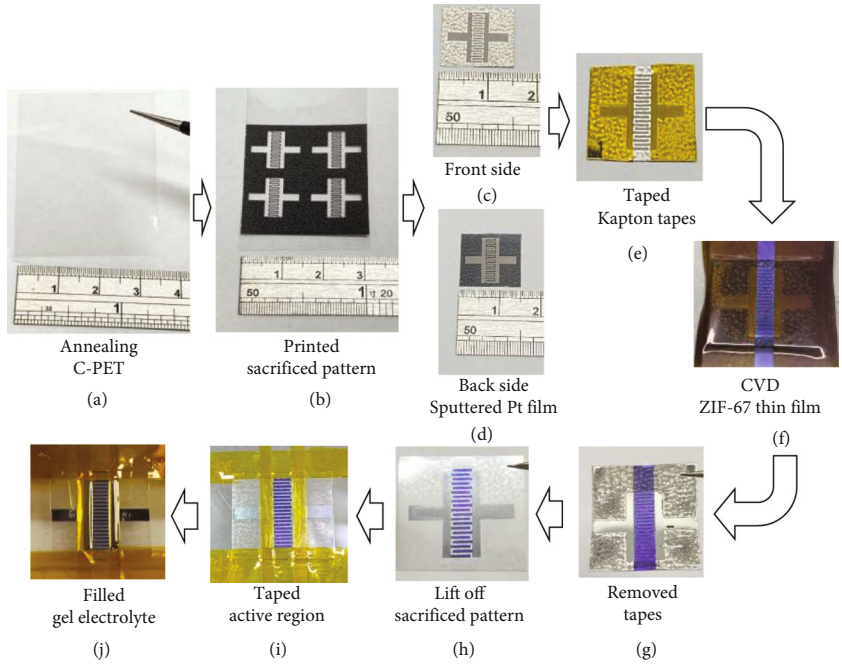

FIGURE 1: Photographs of the fabrication process of ZIF-67 thin films-based all-solid-state flexible interdigital in-planar μSCs. (a) Annealed C-PET, (b) as-printed patterned SPs on C-PET sheet, (c, d) are the front and back sides of as-deposited Pt thin film. (e) Utilization of Kapton tapes to define the ZIF-67 deposition region on Pt film, (f) in situ deposited purple colored ZIF-67 thin film through ultralow temperature CVD process. (g) After the removal of Kapton tape, (h) lift-off process for removing SP layer (including the unwanted Pt/SP and ZIF-67/Pt/SP regions on C-PET) to obtain ZIF-67 thin film onto Pt finger's positions on C-PET. (i) Usage of Kapton tapes to define the finger's positions, (j) filling of NaOH/PVA gel electrolyte between the two electrodes onto the interdigitated-fingers region to obtain the final product of μSC.

used as the flexible substrates. Commercial toner cartridge (Brother TN-450) was utilized for printing the toner sacrificed pattern (SP) layers on the C-PET sheet using a commercial laser printer controlled by a personal computer (PC). Kapton polyimide tape (Guv Team International Co., Ltd., New Taipei City, Taiwan) was used to control the in situ synthesized region of ZIF-67 thin film. Cobalt(II) acetylacetonate (Co(acac)$_2$, $Co(C_5H_7O_2)_2$, ≧99.9%, Sigma Aldrich Co. LLC.) and 2-methylimidazole (2-MIM, $(C_4H_6N_2)_2$, 99%, Sigma Aldrich Co. LLC.) were used as the precursors for the in situ synthesis of ZIF-67 thin films. SP layers were removed by ultrasonic lift-off process using acetone (≧99.8%, I Chemical Co., Ltd., Taiwan). PVA/NaOH-based gel electrolyte was prepared using polyvinyl alcohol (PVA, 98% hydrolyzed, average M.W. 16000, Acros Organics, Belgium) and sodium hydroxide (NaOH, ≧99.9%, Sigma Aldrich Co. LLC.)

2.2. Instruments. An oven (Deng Yng, DOV40, Taiwan) was used for annealing PET sheets. A commercial laser printer (Brother Industries, Ltd., DCP-7060D) was used to print the toner SP on C-PET sheets. Cressington sputter coater 108 (Ted Pella, Inc., U.S.A.) and ultrasonic cleaner D150 (DELTA ULTRASONIC Co., Ltd., New Taipei City, Taiwan) were utilized for Pt sputter and the lift-off process of SP layers, respectively. A home-made CVD equipped with advanced pressure controller (APC, MKS Instruments, U.S.A.) and mass flow controller (MFC, MKS Instruments, U.S.A.) was used for in situ synthesis of ZIF-67 thin films. Deionized (DI) water was produced by the Direct-Q purification system (Merck KGaA). The weight loss measurement of PET and C-PET was carried out using thermogravimetric analyzer (TGA, TA SDT Q600, TA Instruments, U.S.A.). The morphologies and the microstructures of the prepared samples were examined by a scanning electron microscopy (SEM, JEOL, JSM-6330F, Japan). X-ray photoelectron spectroscopy (XPS) studies were conducted using a PHI Quantera SXM/AES 650 (ULVAC-PHI Inc., Japan) with a hemispherical electron analyzer and a scanning monochromated Al Kα X-ray source (hν = 1486.6 eV). X-ray diffraction (XRD, PANalytical X'Pert Pro MPD) using monochromatic high-intensity CuKα radiation (λ = 0.1541 nm) was used to determine the crystalline nature of the specimens and the scanning angle ranged from a 2θ of 5-90° with a scanning rate of 1.6°min^{-1}. The Fourier transform infrared (FTIR, IRSpirit-T, Shimadzu, Japan) spectroscopy was recorded using KBr pellets. Electrochemical measurements were carried out using CHI 660E electrochemical workstation (CH Instruments, Inc., U.S.A.).

2.3. In Situ Synthesis of ZIF-67 Thin Films via ULT CVD. For the in situ synthesis of ZIF-67 thin film, 15 ml of preheated (90°C) DI water, 500 mg 2-MIM and 200 mg Co(acac)$_2$ were used as the condense-phase precursors via the ULT CVD technology at a low temperature of 140°C under Ar atmosphere with a flow of 200 sccm at an atmospheric pressure. The flow of Ar gas and the atmospheric pressure were controlled by MFC and APC, respectively.

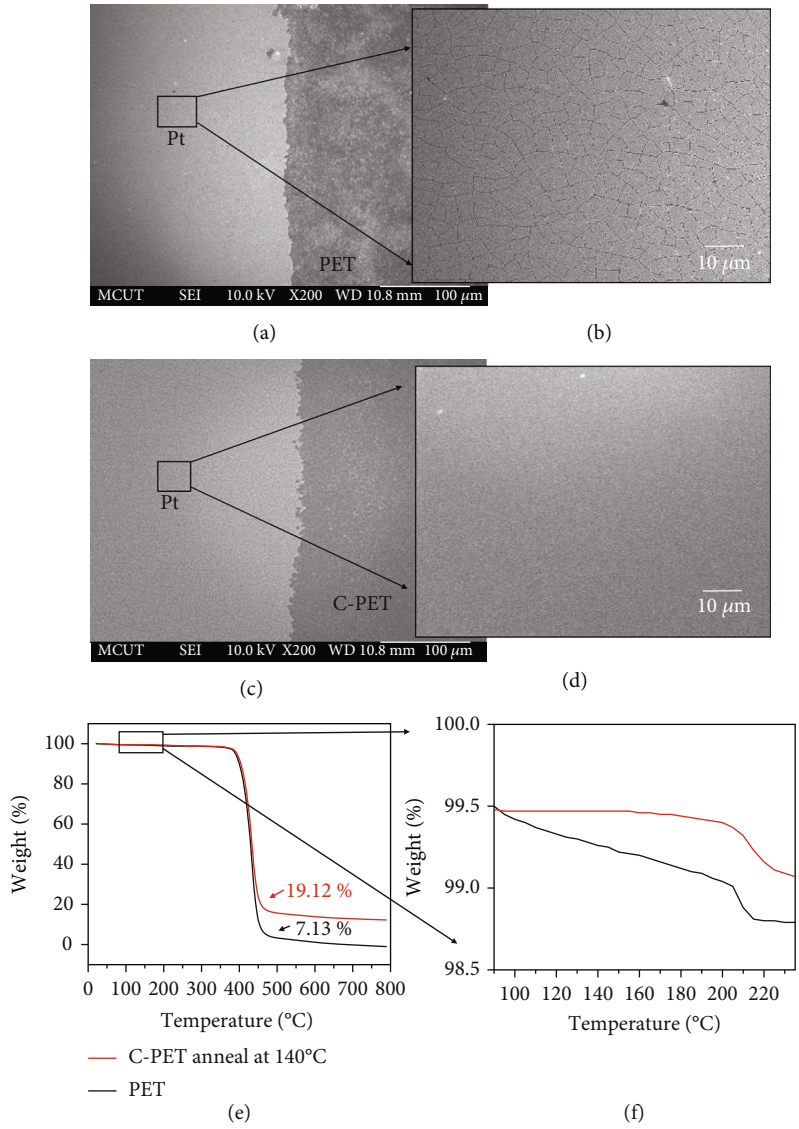

FIGURE 2: Low- and high-magnification SEM images of Pt thin films after CVD process at 140°C and lift-off process (a) on fresh PET sheet, (b) high-magnified image of (a, c) on C-PET sheet, (d) high-magnified image of (c), (e, f) TGA graph and its enlarged curves of fresh PET and C-PET sheets, respectively.

3. Results and Discussion

3.1. Fabrication of ZIF-67 Thin Films-Based Interdigital in-Planar Flexible μSCs. Figure 1 shows the photographs of the fabrication process of ZIF-67 thin films-based flexible all-solid-state interdigital in-planar μSCs. The SP pattern was prepared using laser printer in a similar way of our previous reports [19]. In brief, the processing methods for the fabrication of all-solid-state flexible ZIF-67 thin films-based in-planar interdigital μSC are explained from the following steps. (a) Prior to use, PET sheets were annealed for passivation at 140°C for 12 h in the oven for obtaining recrystallized C-PET in order to improve the antithermal ability of PET, and sequentially cleaned by ultrasonically using detergent, acetone, DI water, and ethanol, and dried at 60°C for 1 h. (b) The designed toner SP was printed on the C-PET sheet using a PC-controlled laser printer; (c, d) are the front and back side images of sputtered Pt thin film with a thickness of 130 nm act as metallic current collectors. (e) Kapton tapes were used to define the region of interdigitated active electrodes and protect the Pt thin-film contact regions during the CVD deposition of ZIF-67 thin film. (f) In situ synthesis of ZIF-67 thin film onto the prepared sample through the ULT CVD method, which is modified from the previous literature [36]. The ULT CVD was used for the in situ synthesis of ZIF-67 thin film, a quartz boat filled with 15 ml of preheated (90°C) DI water, and two independent quartz dishes filled with 500 mg 2-MIM and 200 mg $Co(acac)_2$ were kept separately on another quartz plate, and the as-prepared C-PET sample was put up on the top of the quartz dish of $Co(acac)_2$. Next, the quartz boat (with DI water) and the quartz plate (with 2-MIM, $Co(acac)_2$, and the as-prepared C-PET sample) were sequentially loaded into the quartz tube of the home-made CVD instrument, which already heated to

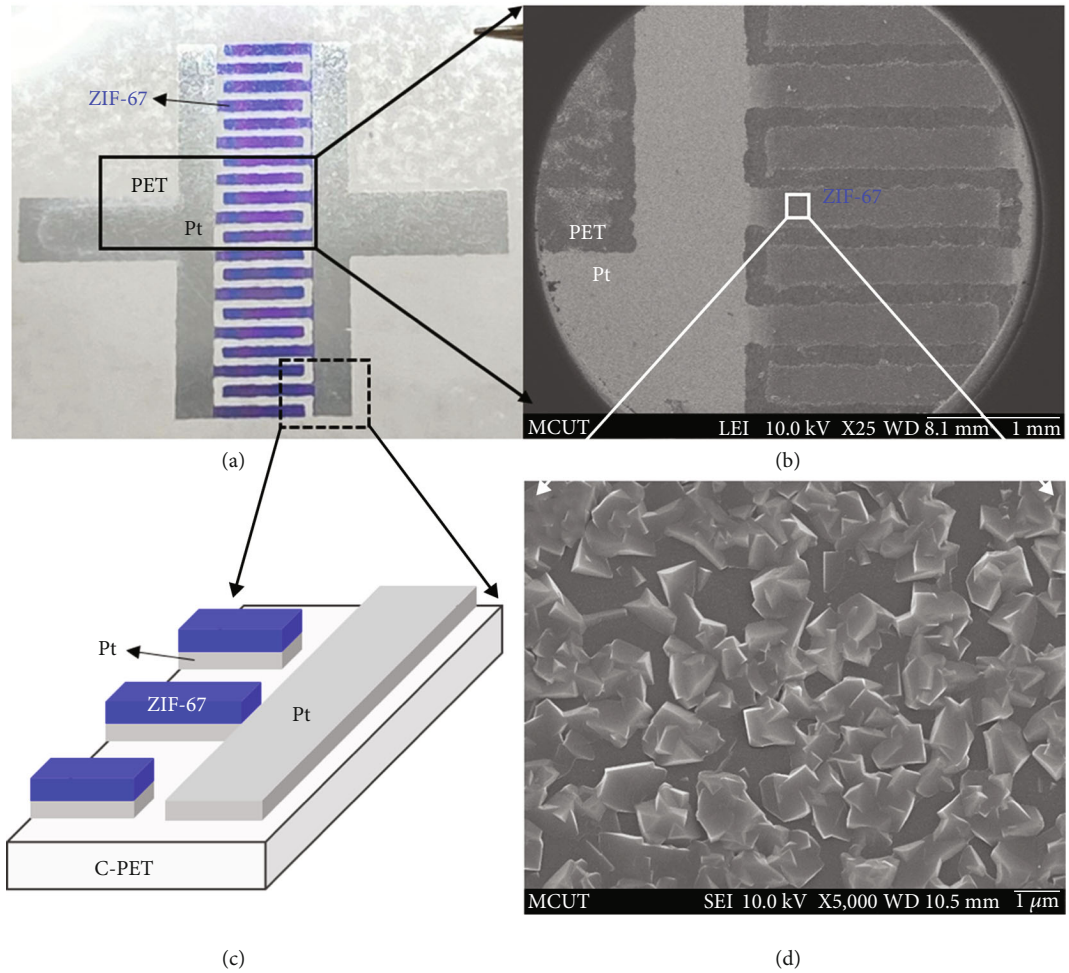

Figure 3: (a) Photographic image of the prepared sample after lift-off process, (b) low-magnification SEM image of the black solid-line box region of (a), (c) high-magnification SEM image of the white solid-line box region in (b), and (d) schematic illustration of μSC configuration with ZIF-67/Pt/C-PET fingers of the dot-line box region in (a).

a constant temperature of 140°C under Ar atmosphere with a flow of 200 sccm at an atmospheric pressure. The ULT CVD process was finished after 10 min, and then the quartz plate was removed from the CVD instrument. (More details are elaborated in Experimental Section in the Supporting Information, the photograph images of ULT CVD configuration for the in situ synthesis of ZIF-67 thin films are shown in Figure S1). A purple color of thin film confirms the formation of ZIF-67 since the purple color coating indicates the unique Co-N chemical bonds with of ZIF-67 as reported in the previous literature [37–39]. (g) After the removal of Kapton tapes, the covered regions show the metallic luster of Pt layers and the uncovered with purple colored long-strip regions show ZIF-67 thin films. (h) The printed SP layer was removed (including the unwanted Pt thin film and ZIF-67/Pt thin film deposited onto the region of SP layer) via the lift off process using the ultrasonic treatment in acetone for 1 min, and then immersed in DI water for 30 sec to remove the residual acetone. The interdigitated active electrodes became visible of purple color, with the transparent gap regions and the measuring contact points of the metallic luster of Pt thin film. (i) Kapton tapes were fixed for defining the interdigitated-fingers region. (j) The fabricated μSC was investigated by employing NaOH/PVA gel electrolyte filled onto the interdigitated-fingers region defined by Kapton tapes, and the gel electrolyte was prepared according to the previous literature [40]. Finally, for the solidification of the electrolyte, NaOH/PVA gel electrolyte was dried overnight at ambient condition and the fabricated μSC was used for the further measurements.

3.2. Morphologies and Composition. The low thermal stable nature of PET sheets restricted their commercial applications. Annealing process is an effective solution for the recrystallization of PET sheets, which enhances their antithermal performance [41]. Accordingly, the purchased PET sheets were annealed for obtaining recrystallized C-PET sheets. Figures 2(c) and 2(d) show the low- and high-magnified SEM images of Pt thin films deposited on the bare PET and C-PET sheets after finishing CVD process step. Obviously, it can be seen from Figure 2(b), Pt thin films of PET sheet substrate cracked seriously; however, the flat morphology of Pt thin films is still maintained on C-PET substrate after annealed CVD

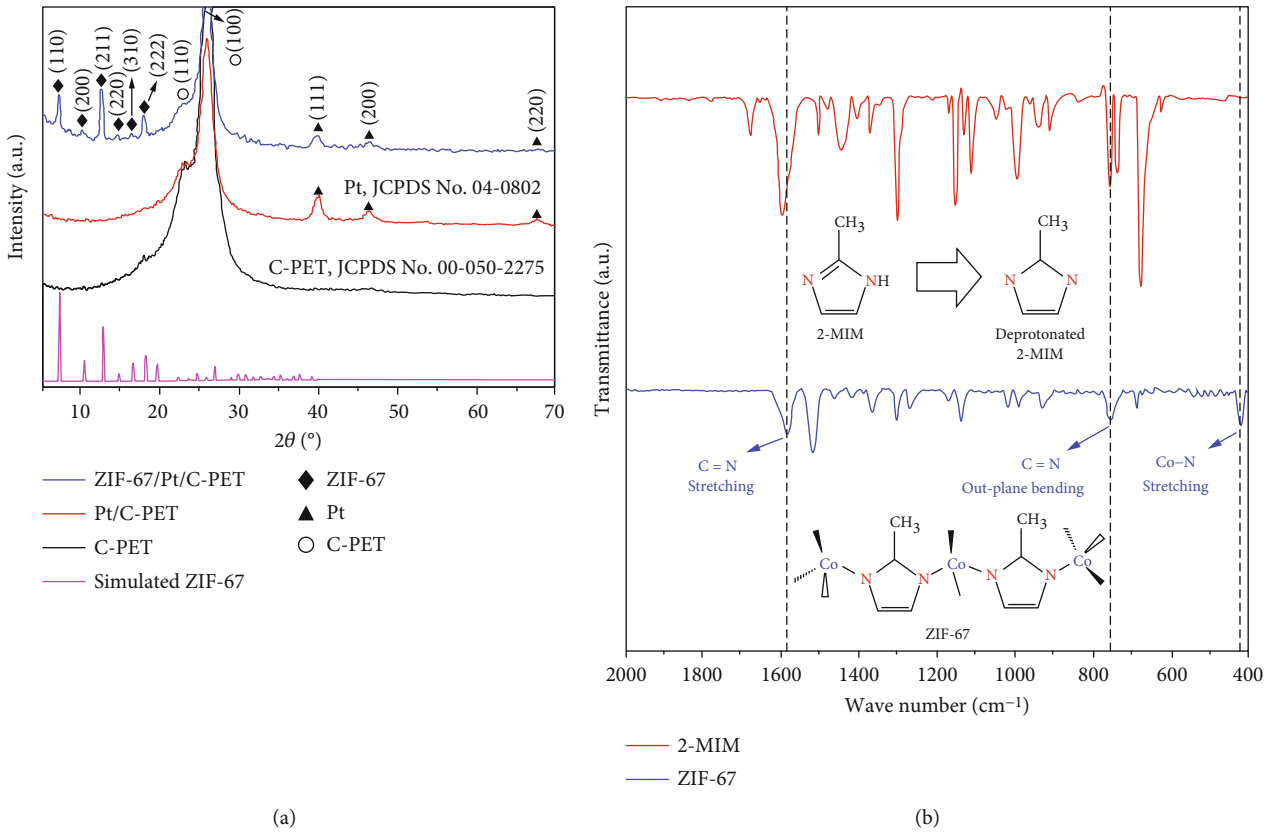

Figure 4: (a) XRD patterns of Pt/C-PET and ZIF-67/Pt/C-PET, (b) FTIR spectrum of 2-MIM and ZIF-67, and the inset shows the crystal structure of deprotonated 2-MIM molecules and ZIF-67.

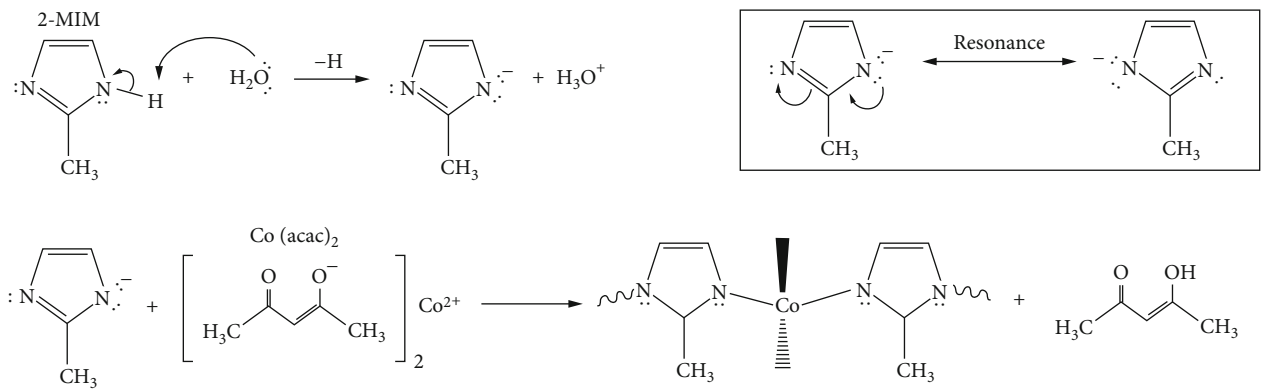

Figure 5: Proposed mechanism for the synthesis of ZIF-67 crystals with water steam.

process step at 140°C. (More details are elaborated in Experimental Section in the Supporting Information; Figure S2 shows the schematic illustration of cracked and uncracked (flat) Pt thin films of PET and C-PET substrate). Pt thin film cracking phenomenon is probably due to the shrinkage of fresh PET surface at high-temperature condition. In order to investigate the antithermal ability of both nonannealed and annealed samples, TGA was performed under N_2 atmosphere at a heating rate of 10°C min^{-1} in the temperature range of 20-800°C. Figure 2(e) shows the TGA curves of PET and C-PET sheets, where C-PET sheet shows high weight retain percentage of 19.12% than that of fresh PET sheet (7.13%) even at high temperature region (>450°C), indicating the superior thermal stability of annealed C-PET than that of nonannealed fresh PET. Figure 2(f) depicts the enlarged curves of Figure 2(e), it clearly shows an almost horizontal curve for C-PET and a declined curve for fresh PET sheet at the temperature range of 100-160°C. Therefore, the annealing process confirmed the passivation performance and improved antithermal ability of C-PET sheet. Accordingly, PET sheets used in this work were annealed at 140°C at an ambient environment for 12 h.

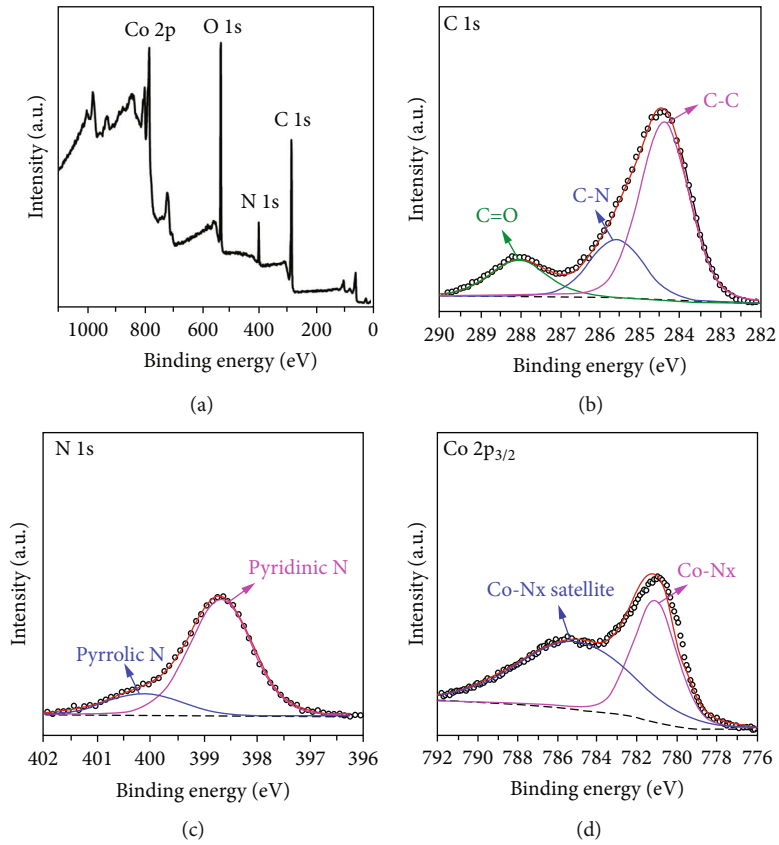

Figure 6: XPS spectra of ZIF-67, (a) survey spectra, (b–d) high-resolution XPS spectra of C 1 s, N 1 s, and Co $2p_{3/2}$, respectively.

Figure 3(a) shows the photographic image of the prepared sample after finishing lift-off process, which is the same image as given in Figure 1(h), where the regions of transparent C-PET, metallic-luster Pt layers, and purple colored ZIF-67 thin films can be clearly identified (Figure 3(d) shows the schematic illustration of the aforementioned regions). Also, this image confirmed the well-intergrown, well-stacked, and the unified surface coverage of ZIF-67 thin films of interdigital fingers. In situ synthesized purple-colored ZIF-67 thin films were stable even after the ultrasonic lift-off process, indicating the highly adhesion behavior of ZIF-67 on C-PET. Consequently, the results verified the successful fabrication of interdigitated electrodes by combining laser printer patterned technology and ultralow temperature CVD ZIF-67 method. Low-magnified SEM image is given in Figure 3(b), which further distinctly identified the regions of C-PET, Pt, and ZIF-67 layers. Figure 3(c) shows the high-magnification SEM image of in situ synthesized ZIF-67 thin film, which confirmed the good crystallinity nature and uniform growth behavior and high-rough surface of ZIF-67. The rough surface of ZIF-67 provides high-surface area, which will be enhanced the rate of electrochemical reactions.

The crystal structure of the in situ synthesized ZIF-67 was examined by XRD and Figure 4(a) shows the XRD patterns of C-PET, Pt/C-PET, and ZIF-67/C-PET samples. XRD of C-PET substrate displays two peaks at 2θ of 22.68° and 26.42°, correspond to (110) and (100) planes of PET (JCPDS card No. 00-050-2275). There are four peaks appeared in the XRD of Pt/C-PET substrate at $2\theta = 39.6°$, 47.4°, 67.1°, and 81.2°, correlate to (111), (200), (220), and (311) planes of Pt (JCPDS card No. 04-0802). In the XRD of ZIF-67, peaks appeared at 2θ of 7.3°, 10.3°, 12.7°, 14.7°, 16.4°, and 18.01°, indicate the planes of (110), (200), (211), (220), (310), and (222), respectively [42]. Hence, XRD results further verified the successful formation of ZIF-67 and its crystallinity, which is consistent with SEM results.

The formation of ZIF-67 is further confirmed by FTIR analysis. Figure 4(b) portrays the FTIR spectra of 2-MIM precursor (red curve) and in situ synthesized ZIF-67 (blue curve). The crystal structure of deprotonated 2-MIM and ZIF-67 is given inside of Figure 4(b), in which C-N bonds of deprotonated 2-MIM are coordinated to Co^{2+} ions. The strong at peak at 431 cm^{-1} is observed due to the Co-N stretching vibration of ZIF-67 framework. The peaks of C=N out-plane bending mode and stretching vibration mode for 2-MIM have appeared at a wavelength of 755 cm^{-1} and 1588 cm^{-1}, respectively, and much lower intensities of those peaks of ZIF-67 confirmed the coordination of Co^{2+} ions with deprotonated 2-MIM [43].

Figure 5 shows the proposed mechanism for the synthesis of ZIF-67 crystals with water steam during CVD process. The gaseous state of water molecules could attack the proton bonded with nitrogen in 2-MIM to form the intermediate product of the deprotonated 2-MIM. Due to the deprotonated 2-MIM owns the equivalent resonance structure, which is able to promote the symmetric coordination

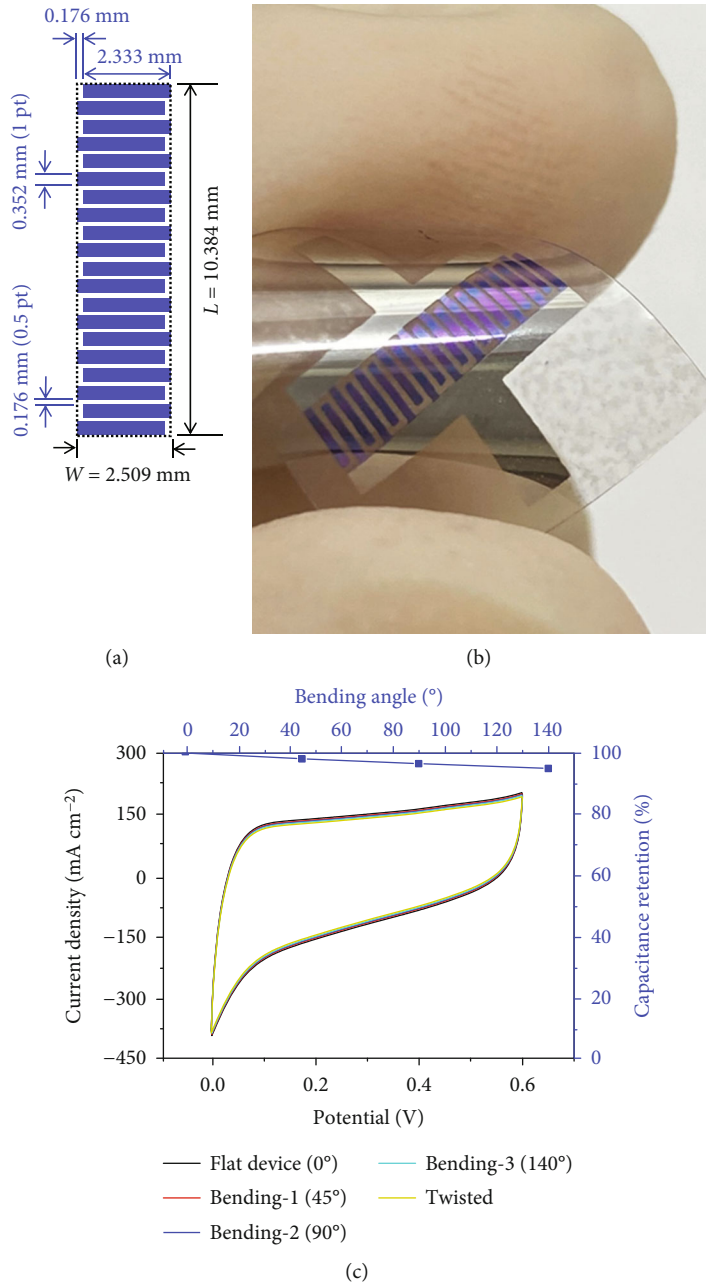

FIGURE 7: (a) Schematic diagram of the measurements of occupied footprint area of μSC (b) photographic image of twisting the as-fabricated ZIF-67-based μSC, (c) CV curves of fabricated μSC measured under different bending conditions at a scan rate of 300 mV s^{-1}.

reactivity with Co2+ ion decomposed from $Co(acac)_2$, thus the formation of ZIF-67 crystals could be quickly deposited onto the substrate surface. (More details are elaborated in Experimental Section in the Supporting Information; Figure S3 shows the comparison of CVD processes with and without using water steam.).

XPS was used to examine the surface structure of in situ synthesized ZIF-67 and its corresponding XPS spectra were shown in Figures 6(a)–6(d). Figure 6(a) demonstrates the XPS survey spectra, displays the characteristic signals of ZIF-67 such as C-N and Co-N bonds, and their satellite peaks. Figure 6(b) shows the deconvoluted spectra of C 1 s, the peaks at 288.1, 285.6, and 284.2 eV, attributed to the C=O, C-N, and C-C bonds, respectively, and the appearance of strong C-N peak is also confirmed from FTIR result of Figure 4(b). Figure 6(c) depicts the high-resolution N 1 s spectra, the two deconvoluted peaks appeared at a binding energy of 398.7 and 400.2 eV, corresponded to pyridinic N and pyrrolic N, bonds, respectively. Figure 6(d) displays the deconvoluted spectra of $Co2p_{3/2}$ the two peaks fitted at 781.2 and 785.4 eV, corresponds to Co-N_x bond and their satellite peak, respectively. The obtained XPS results of ZIF-67 are in good agreement with the previous literatures [39, 44].

3.3. Electrochemical Characterization. The electrochemical performances of as-fabricated μSCs were examined by cyclic

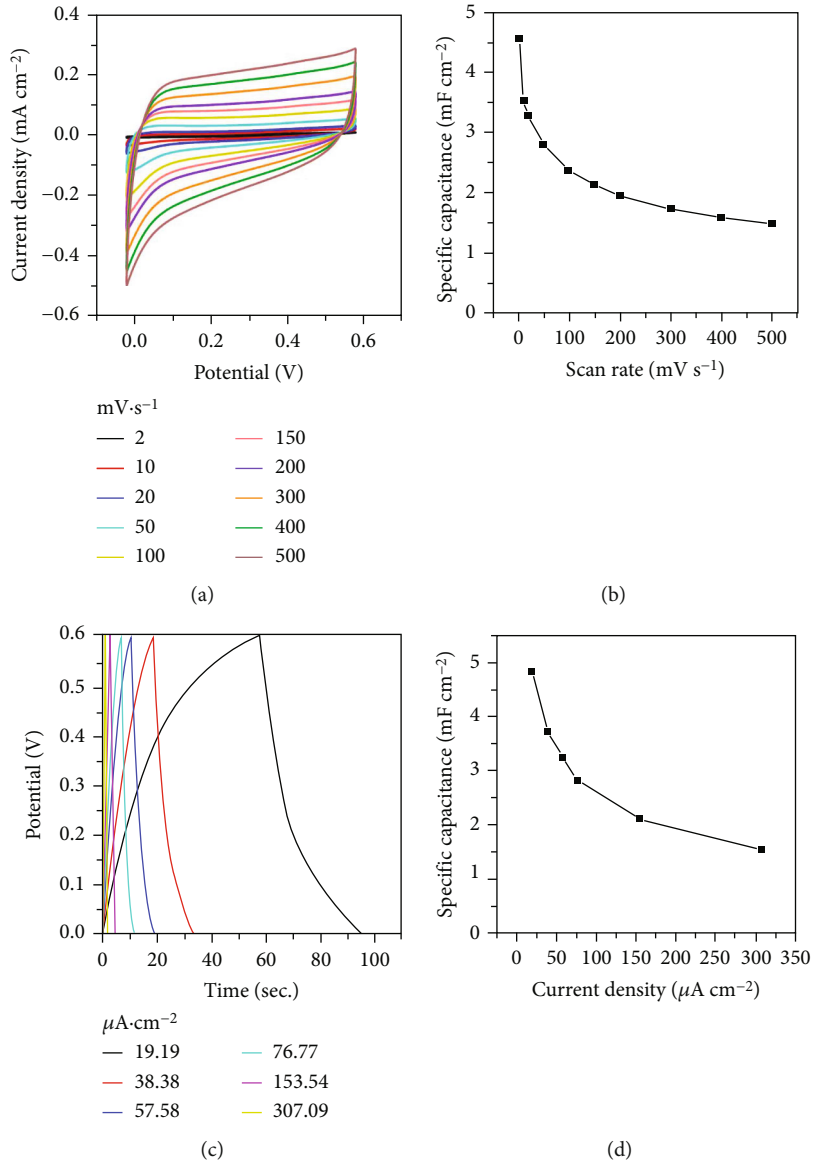

Figure 8: Electrochemical characterization of μSC, (a) CV curves at different scan rates, (b) relationship between calculated C_s from CV curves and various current densities, (c) GCD curves at different current densities, and (d) relationship between calculated C_s from GCD curves and various current densities.

voltammetry (CV) and galvanostatic charge/discharge (GCD) measurements. Figure 7(a) shows the pattern design of our fabricated μSCs and the areal capacitances of fabricated ZIF-67-based μSCs were calculated using the footprint area ($W \times L$) of 26.05 mm^2 (2.509 mm x 10.384 mm), which includes the area of interdigitated electrodes and the gaps (the area measurements are clearly explained in Figure 7(a)). As given in Figure 7(a), the μSC was constructed with 20 fingers (10 fingers per polarity) and it is fixed based on the optimization result of our previous report [21]. In addition, according to the universal printing technology guide rule, the width of each finger and gap are defined as 1 pt (0.352 mm) and 0.5 pt (0.176 mm), respectively, and the length of each finger is 2.333 mm. Figure 7(b) displays the photographic image of the twisted as-fabricated ZIF-67-based μSC. Obviously, due to the utilization C-PET sheet substrate, it demonstrated the outstanding flexibility and also Pt and ZIF thin films are exhibited good adhesion behavior without peeling issue. Besides, the excellent adhesion between Pt films and ZIF-67 thin films can be able to provide low internal resistance. The flexibility of ZIF-67-based μSC was studied using various bending and twisted angle measurements and it will be explained further in detail.

CV curves of fabricated μSC measured at a potential window of 0-0.6 V using NaOH/PVA gel electrolyte at a scan rate of 300 mV s^{-1} under twisted and various bending conditions and their corresponding graph is shown in Figure 7(c). All the measured CV curves exhibited good quasi-rectangular consistency within a wide potential range, indicating a good capacitive behavior even with the gel electrolyte.

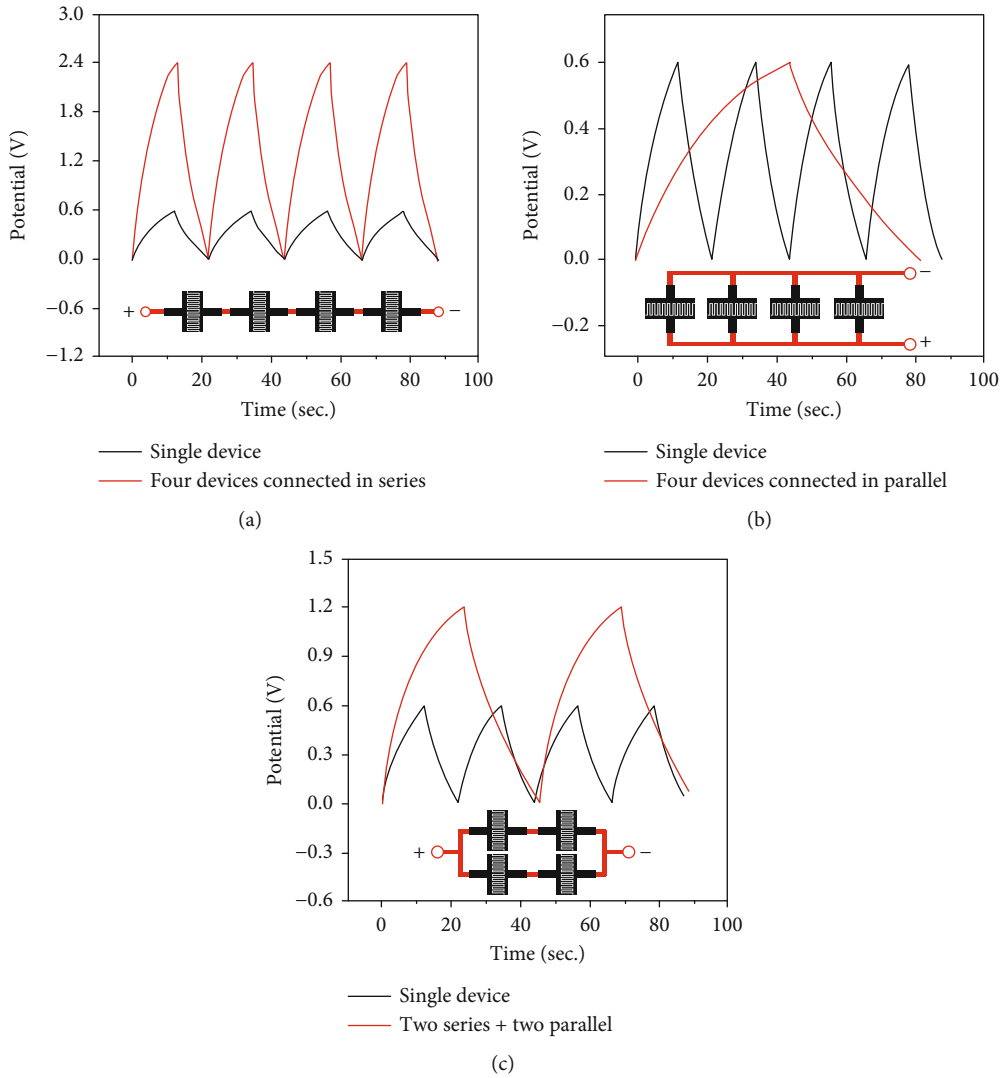

Figure 9: GCD curve and circuit diagrams of (a) 4 μSCs connected in series, (b) 4 μSCs connected in parallel, and (c) the integrated μSCs of 2 series and 2 parallel connected, respectively.

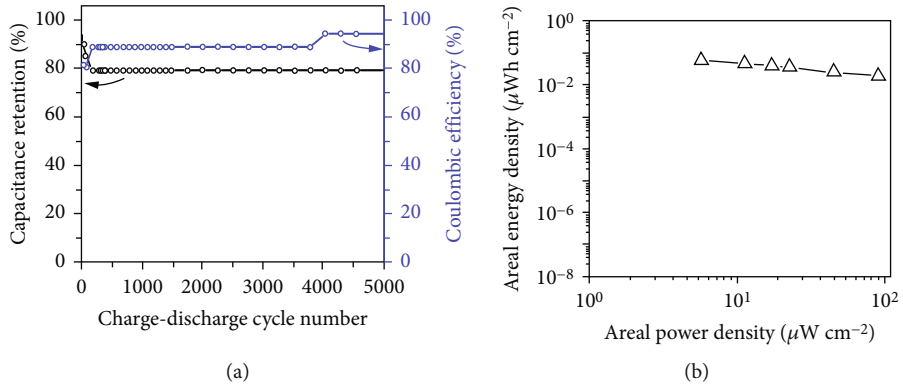

Figure 10: (a) Long-term stability test and (b) Ragone plot of ZIF-67-based μSC.

The calculated capacitance value of all the CV curves is almost same (Figure 7(c)). Fabricated μSC displayed the capacitance retention of 96% even at a higher bending angle of 140°, indicating their excellent mechanically stability, which will be appropriate and essential characteristic for the commercial application of flexible energy storage devices.

Figure 8(a) exhibits the CV curves obtained in a potential range of 0-0.6 V at different scan rates of 2-500 mV s^{-1}. From the CV results, the areal specific capacitance (C_S) of μSC can be estimated by Equation (1) [45, 46]:

$$C_S = \frac{2\int \mathrm{IdV}}{\Delta V \times S}, \quad (1)$$

where I, ΔV, and S are the current density, operating potential window, and scan rate, respectively. The calculated specific capacitance as a function of scan rate is given in Figure 8(b), and the calculated specific capacitances are 4.55 mF cm^{-2} at 2 mV s^{-1}, 3.53 mF cm^{-2} at 10 mV s^{-1}, 3.28 mF cm^{-2} at 20 mV s^{-1}, 2.80 mF cm^{-2} at 50 mV s^{-1}, 2.37 mF cm^{-2} at 100 mV s^{-1}, 2.13 mF cm^{-2} at 150 mV s^{-1}, 1.94 mF cm^{-2} at 200 mV s^{-1}, 1.72 mF cm^{-2} at 300 mV s^{-1}, 1.58 mF cm^{-2} at 400 mV s^{-1}, and 1.48 mF cm^{-2} at 500 mV s^{-1}. To further verify the capacitive properties of the fabricated μSC, GCD studies are conducted under different current densities with an operating potential window of 0.6 V, and their corresponding GCD curves are shown in Figure 8(c). The areal specific capacitance (C_S) of a single electrode from the GCD curves were estimated using

$$C_S = 4\frac{I}{A_{\mathrm{Cell}} \times (\mathrm{dV/dt})}, \quad (2)$$

where I, A_{Cell}, and dV/dt are the current applied, the total effective area of the cell, and the slope of the discharge curve, respectively. The multiplier of 4 adjusts the capacitance of the cell and the combined area of two electrodes to the capacitance and area of a single electrode. Figure 8(d) shows the calculated areal capacitances from the GCD curves at different current densities and the calculated values are 4.85 mF cm^{-2} at 19.19 μA cm^{-2}, 3.74 mF cm^{-2} at 38.39 μA cm^{-2}, 3.26 mF cm^{-2} at 57.57 μA cm^{-2}, 2.84 mF cm^{-2} at 76.77 μA cm^{-2}, 2.11 mF cm^{-2} at 153.54 μA cm^{-2}, and 1.54 mF cm^{-2} at 307.08 μA cm^{-2}. The specific capacitance decreases with the increase in current density, attributed to the limited electrochemical kinetics, which delayed the ion diffusion and thereby reduced the electrode efficiency at high-current densities [47]. The rapid I-V response of discharge process suggested the excellent capacitive performance and high-rate capability, without noticeable iR drop, and the observed voltage drop of GCD curve, suggesting the existence of small equivalent series resistance [48]. Generally, the specific capacitance is not a monotonic function of scan rate or charge-discharge current density. According to the CV and GCD results, the as-fabricated μSCs is maintaining good capacitance retention even at high scan rates and high-current densities, which indicates the excellent electrochemical reversibility and good coulombic efficiency [49].

As shown in Figure 9, the fabricated ZIF-67-based interdigital in-planar μSCs could be integrated in series or parallel connections to increase the output voltage, current, and total capacitance for various requirements of different applications. Herein, we made that 4 μSCs connected in series, 4 μSCs connected in parallel, and the integrated μSCs of 2 series and 2 parallel connections and their corresponding GCD curves and circuit diagrams are given in Figures 9(a)– 9(c), respectively. Series and parallel connected μSCs presented the ideal multiplication results and good repeatability at the same current density.

Long-term stability of fabricated μSC is examined by 5000 consecutive GCD cycles using the potential window of 0-0.6 V at a current density of 1.1 mA cm^{-2} in NaOH/PVA gel electrolyte. Figure 10(a) depicts the graph includes the values of capacitance retention and Coulombic efficiency as a function of cycle number. It can be seen that the capacitance retention of the ZIF-67-based μSC is slowly decreased to ~80% after 300 GCD cycles, this phenomenon probably due to the activation in the first few hundreds of cycles. After that, the capacitance retention is maintained up to 5000 GCD cycles, demonstrating the excellent cycling stability. The Coulombic efficiency is the ratio of the output charge to the input charge, and generally used to quantify the efficiency of an electrochemical energy storage system. The initial Coulombic efficiency is well maintained up to 5000 cycles further illustrating the excellent cycling stability.

The areal energy density ($E_{A,\mathrm{Cell}}$) and power density ($P_{A,\mathrm{Cell}}$) of the μSC are the significant parameters for evaluating the performance of supercapacitors and they can be calculated according to the areal capacitance ($C_{A,\mathrm{Cell}}$) obtained from the GCD measurements. $C_{A,\mathrm{Cell}}$, $E_{A,\mathrm{Cell}}$, and $P_{A,\mathrm{cell}}$ are estimated using Equations ((3)–(5)), respectively [46].

$$C_{A,\mathrm{Cell}} = \frac{C_{,\mathrm{electrode}}}{4}, \quad (3)$$

$$E_{A,\mathrm{Cell}} = \frac{C_{A,\mathrm{cell}} \times V^2}{(2 \times 3600)}, \quad (4)$$

$$P_{A,\mathrm{Cell}} = \frac{E_{A,\mathrm{Cell}} \times 3600}{t}, \quad (5)$$

where V and t are the applied potential and discharge time, respectively. The estimated areal energy density and power density at various current densities are demonstrated in the Ragone plot (Figure 10(b)), ZIF-67-based μSC showed a flat curve in the Ragone plot indicating a small amount of energy loss over a wide range of power densities.

4. Conclusions

In summary, we successfully demonstrated the novel approach by integrating the antithermal behavior of C-PET, laser printer patterning process, and ultralow temperature CVD technology to in situ synthesize ZIF-67 thin films for the fabrication of flexible all-solid-state in-planar ZIF-67-based interdigitated μSCs. The SEM and TGA studies verified the superior antithermal property of the annealed C-PET sheets, assisted for obtaining smooth and flat coating of Pt thin-film current collectors on C-PET surface. Vaporized water steam played an important role in deprotonating the sublimated 2-MIM vapor to assist the coordinating reactions with cobalt ions to form good crystalline ZIF-67 thin

films directly deposited onto substrate surface. The FTIR, XRD, and XPS analyses further confirmed the formation of ZIF-67 and electrochemical measurements exhibited the excellent capacitive behavior of the fabricated ZIF-67-based interdigitated μSCs at high-bending angles, which confirmed the outstanding mechanical stability and flexibility of the fabricated ZIF-67-based interdigitated μSCs. The gas-phase CVD method demonstrates an outstanding strategy for the in situ deposition of MOFs thin films, which is very applicable with microfabrication processes to fabricate microelectronic devices. As a result, compared with the conventional solution-phase synthesized methods, CVD method shows the highly good compatibility to integrate MOFs into miniaturized electronic devices. Therefore, our report shows the great potential features for the fabrication of MOFs thin films-based μSCs and also for other related flexible micropattern fabrication applications.

Data Availability

The data that support the findings of this study are available from the corresponding authors upon reasonable request.

Conflicts of Interest

The authors declare that they have no conflicts of interest.

Authors' Contributions

Kai-Hsiang Lo was responsible in the investigation, methodology, data curation, and writing–original draft. Krishnan Shanmugam Anuratha was assigned in the methodology, data curation, and writing–review and editing. Chia-Chin Cheng worked in the methodology and conceptualization. Shao-Jung Wu helped in the methodology, conceptualization, and data curation. Horng-Yi Juan contributed in the conceptualization and formal analysis. Chia-Hung Su was also assigned in the methodology and data curation. Jeng-Yu Lin was responsible in the validation, resources, and supervision. Chien-Kuo Hsieh worked in the conceptualization, supervision, resources, and writing–review and editing.

Acknowledgments

This study was financially supported by the Ministry of Science and Technology (MOST) of Taiwan (grant/award numbers 110-2221-E-131-012- and 110-2221-E-029-029-MY3).

Supplementary Materials

Figure S1: CVD configuration of in situ synthesis of ZIF-67 thin film. Figure S2: illustration of cracked and uncracked Pt thin film after a heating CVD process, and related SEM images of Pt thin films on nonannealed fresh PET and annealed C-PET. Figure S3: SEM images of CVD ZIF-67 (a) with and (b) without water steam, (c, d) are the CV measured at scan rate of 500 mV s^{-1} and the calculated specific capacitances measured at various scan rates, respectively. *(Supplementary Materials)*

References

[1] H. E. Lee, J. H. Shin, J. H. Park et al., "Micro light-emitting diodes for display and flexible biomedical applications," *Advanced Functional Materials*, vol. 29, no. 24, p. 1808075, 2019.

[2] D. R. Seshadri, R. T. Li, J. E. Voos et al., "Wearable sensors for monitoring the physiological and biochemical profile of the athlete," *npj Digital Medicine*, vol. 2, no. 1, p. 72, 2019.

[3] M. Winter and R. J. Brodd, "What are batteries, fuel cells, and supercapacitors?," *Chemical Reviews*, vol. 104, no. 10, pp. 4245–4270, 2004.

[4] K. Poonam, A. Sharma, S. K. Arora, and S. K. Tripathi, "Review of supercapacitors: materials and devices," *Journal of Energy Storage*, vol. 21, pp. 801–825, 2019.

[5] N. A. Kyeremateng, T. Brousse, and D. Pech, "Microsupercapacitors as miniaturized energy-storage components for on-chip electronics," *Nature Nanotechnology*, vol. 12, no. 1, pp. 7–15, 2017.

[6] B. G. Choi, S.-J. Chang, H.-W. Kang et al., "High performance of a solid-state flexible asymmetric supercapacitor based on graphene films," *Nanoscale*, vol. 4, no. 16, pp. 4983–4988, 2012.

[7] Z. Zheng, M. Retana, X. B. Hu, R. Luna, Y. H. Ikuhara, and W. L. Zhou, "Three-dimensional cobalt phosphide nanowire arrays as negative electrode material for flexible solid-state asymmetric supercapacitors," *ACS Applied Materials & Interfaces*, vol. 9, no. 20, pp. 16986–16994, 2017.

[8] M. F. El-Kady, V. Strong, S. Dubin, and R. B. Kaner, "Laser scribing of high-performance and flexible graphene-based electrochemical capacitors," *Science*, vol. 335, no. 6074, pp. 1326–1330, 2012.

[9] F. N. Dai, X. K. Wang, S. H. Zheng et al., "Toward high-performance and flexible all-solid-state micro-supercapacitors: MOF bulk _vs._ MOF nanosheets," *Chemical Engineering Journal*, vol. 413, p. 127520, 2021.

[10] H. L. Liu, Y. X. Xie, J. X. Li et al., "Laser-induced nitrogen-self-doped graphite nanofibers from cyanate ester for on-chip micro-supercapacitors," *Chemical Engineering Journal*, vol. 404, p. 126375, 2021.

[11] M. F. El-Kady and R. B. Kaner, "Scalable fabrication of high-power graphene micro-supercapacitors for flexible and on-chip energy storage," *Nature Communications*, vol. 4, no. 1, p. 1475, 2013.

[12] Z. S. Wu, K. Parvez, X. L. Feng, and K. Mullen, "Photolithographic fabrication of high-performance all-solid-state graphene-based planar micro-supercapacitors with different interdigital fingers," *Journal of Materials Chemistry A*, vol. 2, no. 22, pp. 8288–8293, 2014.

[13] L. M. Sun, X. H. Wang, K. Zhang, J. P. Zou, and Q. Zhang, "Metal-free SWNT/carbon/MnO_2 hybrid electrode for high performance coplanar micro-supercapacitors," *Nano Energy*, vol. 22, pp. 11–18, 2016.

[14] T. Cheng, Y. W. Wu, Y. L. Chen, Y. Z. Zhang, W. Y. Lai, and W. Huang, "Inkjet-printed high-performance flexible micro-supercapacitors with porous nanofiber-like electrode structures," *Small*, vol. 15, no. 34, p. 1901830, 2019.

[15] J.-K. Chih, A. Jamaluddin, F. Chen, J.-K. Chang, and C.-Y. Su, "High energy density of all-screen-printable solid-state micro-supercapacitors integrated by graphene/CNTs as hierarchical electrodes," *Journal of Materials Chemistry A*, vol. 7, no. 20, pp. 12779–12789, 2019.

[16] H. L. Liu, Y. X. Xie, J. B. Liu et al., "Laser-induced and KOH-activated 3D graphene: a flexible activated electrode fabricated via direct laser writing for in-plane micro-supercapacitors," *Chemical Engineering Journal*, vol. 393, p. 124672, 2020.

[17] J. Jung, J. R. Jeong, J. Lee et al., "In situ formation of graphene/metal oxide composites for high-energy microsupercapacitors," *NPG Asia Materials*, vol. 12, no. 1, 2020.

[18] H. B. Hu, K. Zhang, S. X. Li, S. L. Jia, and C. H. Ye, "Flexible, in-plane, and all-solid-state micro-supercapacitors based on printed interdigital Au/polyaniline network hybrid electrodes on a chip," *Journal of Materials Chemistry A*, vol. 2, no. 48, pp. 20916–20922, 2014.

[19] K. C. Huang, C. H. Lin, K. S. Anuratha et al., "Laser printer patterned sacrificed layer for arbitrary design and scalable fabrication of the all-solid-state interdigitated in-planar hydrous ruthenium oxide flexible micro supercapacitors," *Journal of Power Sources*, vol. 417, pp. 108–116, 2019.

[20] Y. Wang, Y. Zhao, and L. T. Qu, "Laser fabrication of functional micro-supercapacitors," *Journal of Energy Chemistry*, vol. 59, pp. 642–665, 2021.

[21] W. Y. Lee, T. K. Chuang, and C. K. Hsieh, "Enhanced capacitance of hydrous ruthenium oxide based all-solid-state interdigital in-planar micro-supercapacitors," *Electrochimica Acta*, vol. 317, pp. 312–321, 2019.

[22] H. Furukawa, K. E. Cordova, M. O'Keeffe, and O. M. Yaghi, "The chemistry and applications of metal-organic frameworks," *Science*, vol. 341, no. 6149, p. 974, 2013.

[23] D. Y. Lee, S. J. Yoon, N. K. Shrestha, S.-H. Lee, H. Ahn, and S.-H. Han, "Unusual energy storage and charge retention in Co-based metal-organic- frameworks," *Microporous and Mesoporous Materials*, vol. 153, pp. 163–165, 2012.

[24] D. Y. Lee, D. V. Shinde, E.-K. Kim et al., "Supercapacitive property of metal-organic-frameworks with different pore dimensions and morphology," *Microporous and mesoporous materials*, vol. 171, pp. 53–57, 2013.

[25] K.-B. Wang, Q. Xun, and Q. Zhang, "Recent progress in metal-organic frameworks as active materials for supercapacitors," *EnergyChem*, vol. 2, no. 1, article 100025, 2020.

[26] T. Ma, H. Li, J.-G. Ma, and P. Cheng, "Application of MOF-based materials in electrochemical sensing," *Dalton Transactions*, vol. 49, no. 47, pp. 17121–17129, 2020.

[27] Y. Xu, Q. Li, H. Xue, and H. Pang, "Metal-organic frameworks for direct electrochemical applications," *Chemical Reviews*, vol. 376, pp. 292–318, 2018.

[28] B. Chen, Z. Yang, Y. Zhu, and Y. Xia, "Zeolitic imidazolate framework materials: recent progress in synthesis and applications," *Journal of Materials Chemistry A*, vol. 2, no. 40, pp. 16811–16831, 2014.

[29] A. M. Mohamed, M. Ramadan, and N. K. Allam, "Recent advances on zeolitic imidazolate -67 metal-organic framework-derived electrode materials for electrochemical supercapacitors," *Journal of Energy Storage*, vol. 34, article 102195, 2021.

[30] G. Zhong, D. Liu, and J. Zhang, "The application of ZIF-67 and its derivatives: adsorption, separation, electrochemistry and catalysts," *Journal of Materials Chemistry A*, vol. 6, no. 5, pp. 1887–1899, 2018.

[31] M. Wang, Y. Feng, Y. Zhang et al., "Ion regulation of hollow nickel cobalt layered double hydroxide nanocages derived from ZIF-67 for high-performance supercapacitors," *Applied Surface Science*, vol. 596, article 153582, 2022.

[32] L. Wang, Z. Zhang, Q. Han et al., "Preparation of CdS-P25/ZIF-67 composite material and its photocatalytic CO_2 reduction performance," *Applied Surface Science*, vol. 584, article 152645, 2022.

[33] Q. Shi, Z. F. Chen, Z. W. Song, J. P. Li, and J. X. Dong, "Synthesis of ZIF-8 and ZIF-67 by steam-assisted conversion and an investigation of their tribological behaviors," *Angewandte Chemie. International Edition*, vol. 50, no. 3, pp. 672–675, 2011.

[34] I. Stassen, M. Styles, G. Grenci et al., "Chemical vapour deposition of zeolitic imidazolate framework thin films," *Nature Materials*, vol. 15, no. 3, pp. 304–310, 2016.

[35] Y. Li, H. Q. Xie, J. Li, Y. Bando, Y. Yamauchi, and J. Henzie, "High performance nanoporous carbon microsupercapacitors generated by a solvent-free MOF-CVD method," *Carbon*, vol. 152, pp. 688–696, 2019.

[36] J. K. Huang, N. Saito, Y. C. Cai et al., "Steam-assisted chemical vapor deposition of zeolitic imidazolate framework," *ACS Materials Letters*, vol. 2, no. 5, pp. 485–491, 2020.

[37] D. Matatagui, A. Sainz-Vidal, I. Gracia, E. Figueras, C. Cane, and J. M. Saniger, "Chemoresistive gas sensor based on ZIF-8/ZIF-67 nanocrystals," *Sensors and Actuators B: Chemical*, vol. 274, pp. 601–608, 2018.

[38] J. Ethiraj, S. Palla, and H. Reinsch, "Insights into high pressure gas adsorption properties of ZIF-67: experimental and theoretical studies," *Microporous and Mesoporous Materials*, vol. 294, article 109867, 2020.

[39] S. Dou, C.-L. Dong, Z. Hu et al., "Atomic-scale CoOx species in metal–organic frameworks for oxygen evolution reaction," *Advanced Functional Materials*, vol. 27, no. 36, article 1702546, 2017.

[40] A. C. Lokhande, A. Patil, A. Shelke et al., "Binder-free novel Cu_4SnS_4 electrode for high-performance supercapacitors," *Electrochimica Acta*, vol. 284, pp. 80–88, 2018.

[41] K. Shinotsuka, V. N. Bliznyuk, and H. E. Assender, "Near-surface crystallization of PET," *Polymer*, vol. 53, no. 24, pp. 5554–5559, 2012.

[42] L. Meng, B. Yu, and Y. Qin, "Templated interfacial synthesis of metal-organic framework (MOF) nano- and micro-structures with precisely controlled shapes and sizes," *Communications Chemistry*, vol. 4, no. 1, p. 82, 2021.

[43] Z. Öztürk, M. Filez, and B. M. Weckhuysen, "Decoding nucleation and growth of zeolitic imidazolate framework thin films with atomic force microscopy and vibrational spectroscopy," *European Journal*, vol. 23, no. 45, pp. 10915–10924, 2017.

[44] A. M. Kale, R. Manikandan, C. J. Raj, R. Velayutham, W.-J. Cho, and B. C. Kim, "Post synthetic annealing of zeolitic imidazolate framework-67 for high- performance hybrid supercapacitors," *Applied Surface Science*, vol. 542, article 148716, 2021.

[45] M. D. Stoller and R. S. Ruoff, "Best practice methods for determining an electrode material's performance for ultracapacitors," *Energy & Environmental Science*, vol. 3, no. 9, pp. 1294–1301, 2010.

[46] L. Li, J. B. Zhang, Z. W. Peng et al., "High-performance pseudocapacitive microsupercapacitors from laser-induced graphene," *Advanced Materials*, vol. 28, no. 5, pp. 838–845, 2016.

[47] F. Wolfart, D. P. Dubal, M. Vidotti, and P. Gomez-Romero, "Hybrid core-shell nanostructured electrodes made of polypyrrole nanotubes coated with Ni(OH)2nanoflakes for high energy-density supercapacitors," *RSC Advances*, vol. 6, no. 18, pp. 15062–15070, 2016.

[48] M. K. Hota, Q. Jiang, Y. Mashraei, K. N. Salama, and H. N. Alshareef, "Fractal electrochemical microsupercapacitors," *Advanced Electronic Materials*, vol. 3, no. 10, 2017.

[49] Z. J. Fan, J. Yan, T. Wei et al., "Asymmetric supercapacitors based on graphene/MnO2 and activated carbon nanofiber electrodes with high power and energy density," *Advanced Functional Materials*, vol. 21, no. 12, pp. 2366–2375, 2011.